Modeling Earth Systems and Environment (2023) 9:2993–3008
https://doi.org/10.1007/s40808-022-01595-0

SHORT COMMUNICATION

Modelling soil stability in wide tunnels using FELA and multivariate adaptive regression splines analysis

Van Qui Lai[1,2] · Jim Shiau[3] · Thanachon Promwichai[4] · Suchart Limkatanyu[5] · Rungkhun Banyong[4] · Suraparb Keawsawasvong[4]

Received: 11 September 2022 / Accepted: 28 October 2022 / Published online: 15 December 2022

Abstract
Stability evaluations of soil or rock excavation are significantly affected by the shape of the underground cavity. Whilst most of the previous stability research was in circular tunnelling problems, rectangular tunnels are nevertheless seldom studied even though the latter is gaining more popularity in practices, especially in railway engineering. The purpose of the technical note is to bridge the current research gap using the robust lower and upper bound finite element limit analysis to study the undrained stability of wide rectangular tunnels in cohesive soils under both collapse and blowout scenarios in two-dimensional conditions. A dimensionless stability number is presented to define the solution and the associated failure mechanisms are examined with three distinct types of mechanisms. In addition, a machine learning model, namely, multivariate adaptive regression splines (MARS), is used to develop design equations for evaluating soil stability. The findings in this study provide a reliable solution to improve the current design standard for the stability of rectangular underground spaces in undrained clays.

Keywords Stability analysis · Wide rectangular tunnel · Limit analysis · MARS

✉ Suraparb Keawsawasvong
ksurapar@engr.tu.ac.th

Van Qui Lai
lvqui@hcmut.edu.vn

Jim Shiau
jim.shiau@usq.edu.au

Thanachon Promwichai
thanachon.pr@outlook.co.th

Suchart Limkatanyu
suchart.l@psu.ac.th

Rungkhun Banyong
rungkhun.ban@gmail.com

1 Faculty of Civil Engineering, Ho Chi Minh City University of Technology (HCMUT), 268 Ly Thuong Kiet Street, District 10, Ho Chi Minh City, Vietnam

2 Vietnam National University Ho Chi Minh City (VNU-HCM), Linh Trung Ward, Thu Duc District, Ho Chi Minh City, Vietnam

3 School of Engineering, University of Southern Queensland, Toowoomba, QLD 4350, Australia

4 Department of Civil Engineering, Thammasat School of Engineering, Thammasat University, Pathumthani 12120, Thailand

5 Department of Civil and Environmental Engineering, Faculty of Engineering, Prince of Songkla University, Songkhla, Thailand

Introduction

Underground soil or rock excavations such as for tunnelling and mining applications require substantial effort in the evaluation of soil stability at various design stages of excavation. Such a stability evaluation can be significantly affected by its shape, as required by the need in maximizing the underground space. Indeed, a tunnel boring machine (TBM) is an efficient and effective tool for excavating a circular tunnel and it has been used widely in the past few decades (Jamshidi 2018). Nevertheless, underground excavation work that is rectangular or square is more difficult to build and very few research on stability evaluation were reported. Despite this, the use of rectangular underground spaces has become more and more popular in recent years in railway engineering (Yatsumoto et al. 2019; Vinod and Khabbaz 2019; Soleiman Dehko et al. 2019; Chen et al., 2021).

The stability of tunnels in cohesive, cohesive-frictional, and cohesionless soils has been the subject of numerous scientific studies. Published literatures on the stability problem of circular tunnels in cohesionless and frictional soil may include several researchers such as (Mühlhaus 1985; Leca and Dormieux 1990; Chambon and Corté 1994; Mollon et al. 2009, 2010; Zhang et al. 2017; Shiau et al. 2021a). In recent years, elliptical tunnels have been a study subject by several other researchers (Shiau et al. 2021a, b). Among these investigated in cohesionless soil tunnels, the upper bound limit analysis was performed except for Mühlhaus (1985) who employed the lower bound limit analysis method for the first time in this field of problem.

Since the advanced development of limit analysis with finite elements and mathematical programming, several researchers focused on simulating the various forms of tunnels in cohesive and cohesive-frictional soils, including circular tunnels (e.g., Sloan and Assadi 1993; Wilson et al. 2011; Yamamoto et al. 2011; Sahoo and Kumar 2014), elliptical tunnels (e.g., Yang et al. 2015) and square/rectangular tunnels (e.g., Assadi and Sloan 1991; Abbo et al. 2013; Wilson et al. 2013). The latest stability problem of square/rectangular tunnels in cohesionless soil was carried out by Dutta and Bhattacharya (2019) by employing the lower bound finite element limit analysis approaches to determine the lining support pressure inside the tunnels. It is to be noted that no published literature on the undrained stability problem of a wide rectangular tunnel in cohesive soil can be found. Collapse failure (downward movement) and blowout failure (upward movement) are the two main modes of tunnel failure. The self-weight of a soil mass and ground surcharge pressures are two critical components connected to collapse failures, whereas blowout failures are only due to external forces exerted against the soil weight (Shiau and Al-Asadi 2018; 2020a, b; 2021, 2022a, b). However, most stability studies of rectangular tunnels were on the "collapse" side, none of the blowout studies can be found in the literature.

The aim of this study is to apply the rigorous upper and lower bound finite element limit analysis (FELA) method in conjunction with the Tresca yield criterion to investigate the undrained stability of wide rectangular tunnels in cohesive soils under both collapse and blowout situations. Numerical results obtained from FELA are represented by a dimensionless stability number that is a function of the cover to depth ratio and the width to depth ratio. Furthermore, the numerical results are used as the artificial set of data for a machine learning MARS model ~ multivariate adaptive regression splines. MARS is capable of effectively capturing the nonlinear interactions between a set of input variables and output variables in multiple dimensions as well as evaluating the associated sensitivities. The MARS-based sensitivity analysis and design equations for predicting the limit state solutions of rectangular tunnel stability provide a reliable evaluation of factor of safety (*FOS*) that can be used by designers in their preliminary design.

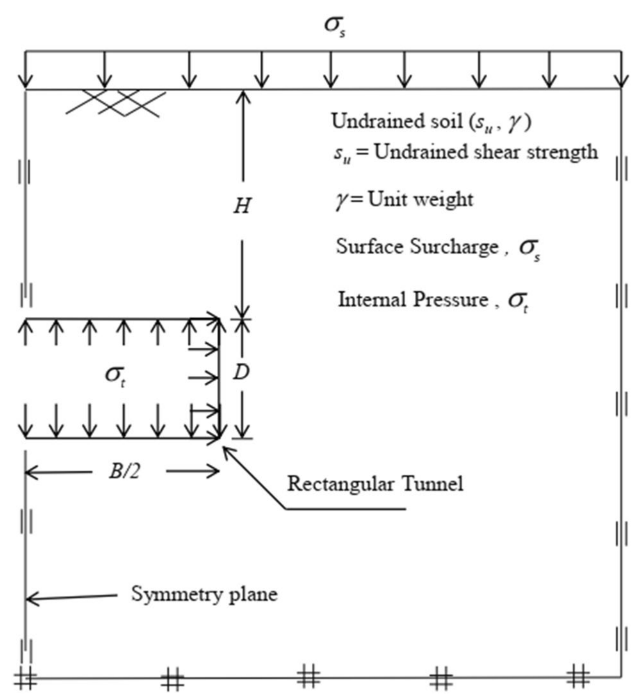

Fig. 1 Rectangular tunnel in symmetry condition-problem definition

Problem statement

The problem statement of a wide rectangular tunnel with a symmetric plane is shown in Fig. 1. The wide rectangular tunnel in undrained clay can be reasonably determined under plane strain conditions with a width B, a height D, and a cover depth H, because of the large length in a longitudinal direction. Both the surface surcharge (σ_s) and the internal support pressure (σ_t) are considered as positive compressive pressures. The soil mass around the tunnel is assumed to be a perfectly rigid plastic material and is considered as homogenous and isotropic with the Tresca yield criterion. The soil material property is represented by the undrained shear strength (S_u) and the soil unit weight (γ). The critical stability number approach (Broms and Bennermark 1967) in conjunction with the dimensionless technique is used to compute the stability solutions of rectangular tunnels in cohesive soil. The critical stability number (N_c) is shown in Eq. (1).

$$N_c = \frac{\sigma_s + \gamma H - \sigma_t}{S_u} = f\left(\frac{H}{D}, \frac{B}{D}\right). \tag{1}$$

Equation (1) combines the surcharge (σ_s), the soil self-weight (γH), and the support pressure (σ_t), and it is a function of the two geometrical design parameters i.e., *H/D* and *B/D*. Where N_c denotes the critical stability number of rectangular tunnels, *H/D* denotes the cover to depth ratio, and *B/D* denotes the width to depth ratio. Equation (1) is applicable to undrained analysis with soil internal friction angle $\phi_u = 0$.

Since N_c is the dimensionless critical stability number, the input parameters such as σ_s, γ, and S_u in Eq. (1) are arbitrary constants. Thus, the objective of the limit solution in this study is to determine the critical support pressure σ_t that would result in either a collapse or a blowout scenario. A positive unit compressive pressure σ_t is initiated for a blowout solution, whilst an opposite direction (i.e., negative tensile unit pressure) is given to obtain a "collapse" solution. The obtained σ_t is then substituted back into Eq. (1) to compute the critical stability number $N_{c.}$ The range of investigation of the design parameters (*H/D* and *B/D*) are selected as *H/D* = 1–10 and *B/D* = 1–10.

Numerical modelling

This technical note utilized OptumG2 (Krabbenhoft et al. 2015) with rigorous finite element upper and lower bounds techniques to find out the stability solutions of rectangular tunnels in undrained clayey soils. The results produced using this approach are accurate and can bracket the true solution from above and below in a very tight bound. Unlike some other upper bound analytical approaches, finite element limit analysis does not require any assumptions about the failure surface in advance. This FELA technique has been effectively used to study several geotechnical stability structures under varied stress circumstances (Shiau et al. 2004, 2006 Sloan 2013).

According to the UB formulation, the clay is discretized into six-noded triangular elements with velocity components at all nodes. The kinematically admissible velocity field is to be found everywhere in the domain as well as at the boundary conditions. The load is calculated from the principle of virtual work based on compatibility and the flow rule formulations. As a result, the support pressure is related to

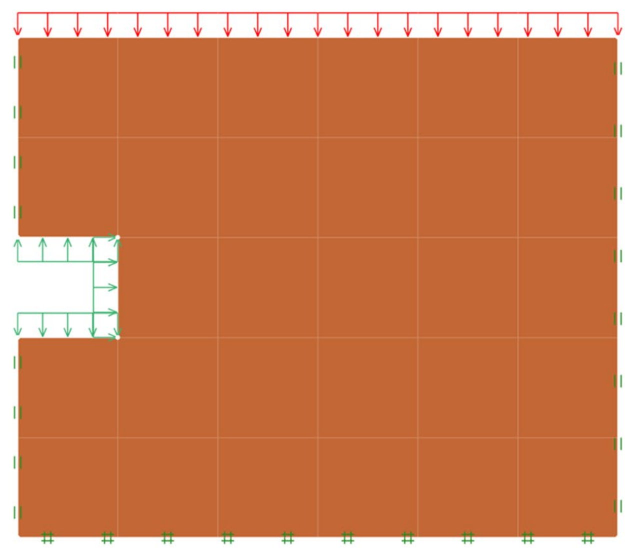
(a)

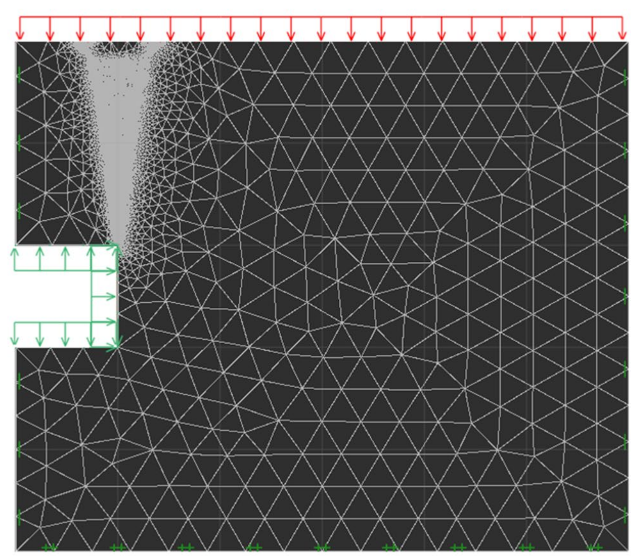
(b)

Fig. 2 **a** Numerical model and **b** Typical adaptive mesh the problem's unknown velocities using the virtual work, which compares the rate of work done between external loads to the internal energy dissipation at triangle components. On the other hand, in the LB formulation, the clay around the tunnel is divided into several three-nodded linear triangular elements, with three unknown stress components at each node. Note that stress discontinuities are allowed to the lower bound mesh at common edges of neighboring triangular elements. The objective function in the optimization is to maximize the support pressure (σ_t) of the tunnel while taking into account the statically permissible stress constraints, such as element equilibrium, stress discontinuities, stress boundary conditions, as well as failure criterion.

The numerical model of the rectangular tunnel generated by OptumG2 is shown in Fig. 2a for half of the tunnel due to the problem symmetry. A standard boundary condition is employed for all the analyzes considered in the paper. A fully fixed condition is applied at the base while the nodes at the left and right boundary are free to move in the vertical direction only i.e., soil movements in the normal direction are prevented. Two free surfaces are noted; being the top ground surface and the inner tunnel surface. The sizes of model domains were carefully chosen and tested to ensure that the plastic yield zone development has no influence on the solution. It is also imperative to ensure the overall velocity field is distributed within the boundary to avoid any inaccuracy that may arise owing to the mesh domain selection. Note that both collapse and blowout scenarios are studied in the paper. Technically speaking, to obtain a "blowout" solution, it is necessary to change the pressure direction of σ_t in the objective function. More discussion of the solution process are presented in the next section. Also, note that the numerical models of the rectangular tunnel in this study are the original model.

A typical final adaptive mesh of this problem is shown in Fig. 2b. For all analyses, the adaptive mesh functionality and optimization features are engaged. This adaptive feature would improve the solution accuracy as the mesh density is the greatest in zones with significant plastic shear strains. This study utilizes five iterations of adaptive meshing, with the number of components gradually increasing from 5000 to 10,000 throughout the course of the five repetitions. It is important to note that the resulting adaptive mesh resembles a failure mechanism with non-zero shear power dissipation (Yodsomjai et al. 2021).

Numerical results

A series of stability numbers of this problem are produced using a set of input parameters including (B, D, σ_s, γ, H, and S_u) in both blowout and collapse analyses. The range of investigation of the design parameters (H/D and B/D) are

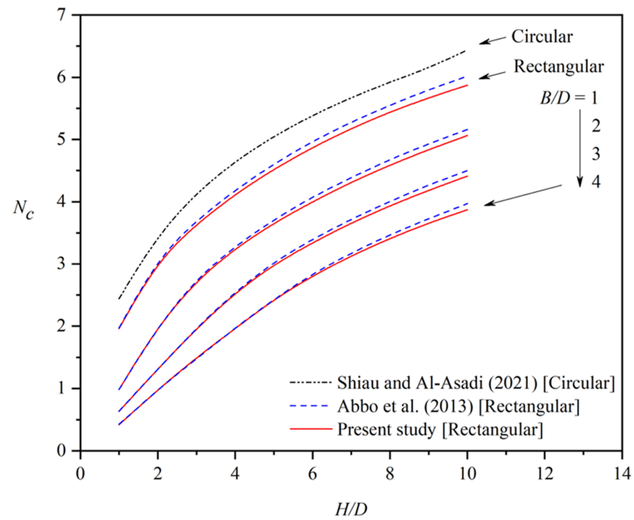

Fig. 3 Comparison of upper bound N_c result between the present study and previous study

selected as $H/D = 1$–10 and $B/D = 1$–10. Note that a positive unit compressive pressure σ_t is initiated for a blowout solution, whilst a negative tensile unit pressure is given to obtain a "collapse" solution. The ultimate limit solution is to determine the critical tunnel pressure σ_t that would be substituted back to Eq. (1) to compute the critical stability number N_c. The determined N_c results are compared and verified with previously published solutions in the following sections.

Verification

To verify the computed FELA solutions, numerical comparison of N_c between the present results and those by Abbo et al. (2013) is shown in Fig. 3. Note that the results in Fig. 3 are all tunnels under collapse failure. There were no existing solutions of N_c for blowout cases of rectangular tunnels in the past. Thus, only the upper bound solutions are used in this comparison. Numerical N_c results have shown that the two solutions are in good agreement for the considered range of $H/D = 1$–10 and $B/D = 1$–4. This has indicated that the current FELA solutions are accurate and the comparison has provided a high level of confidence in all later parametric analyses. In addition, the results of N_c for circular tunnels by Shiau and Al-Asadi (2021) are employed in Fig. 3. It can be seen that the circular tunnel has greater stability than that of the square tunnel ($B/D = 1$) for all values of H/D. This is due to the circular shape having a larger arching effect than the rectangular shape with square corners.

Parametric studies

Shown in Fig. 4 is the variation of critical stability number N_c with the increasing depth ratio (H/D) for the various

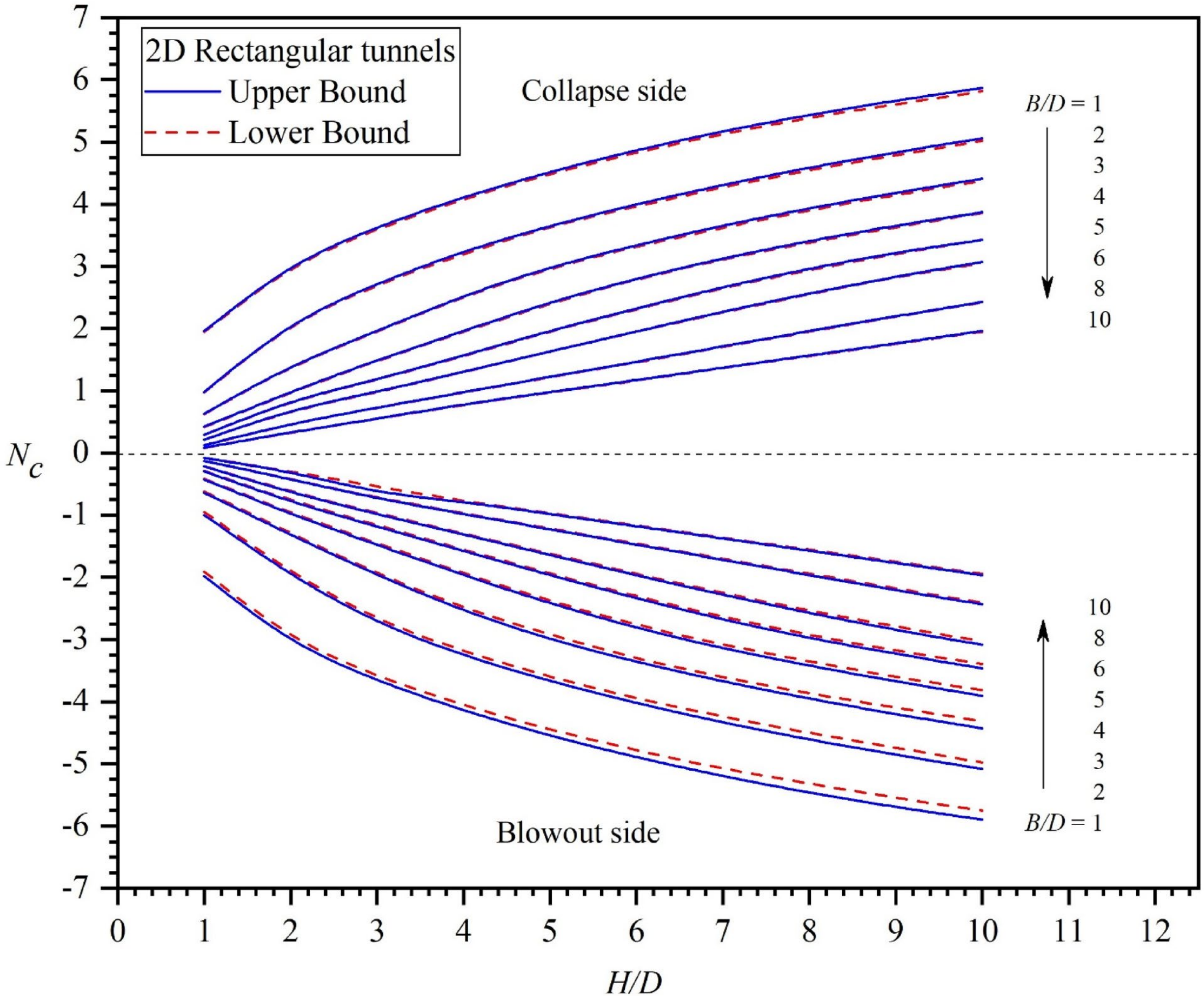

Fig. 4 N_c results for collapse and blowout (*H/D* = 1–10, *B/D* = 1–10)

width ratio *B/D* = 1–10. On the positive N_c collapse side, the value of N_c increases nonlinearly with the increase in *H/D* for all values of *B/D*. The larger the *B/D* value, the wider the rectangular tunnel, and the smaller the critical stability number N_c. Also, note that the curve transformation from nonlinear to linear as the value of *B/D* increases (*B/D* = 10). On the blowout side, negative values of N_c are presented. This can be understood from Eq. (1), in that, the inner pressure σ_t must be greater than the combined download pressure ($\sigma_s + \gamma H$). In such blowout cases, the resulting values of N_c are negative. It is not surprised to note that symmetrical results are obtained in the undrained blowout study. The same blowout discussions can, therefore, be made as those for the collapse scenario, i.e., the larger the *B/D* value, the wider the rectangular tunnel, and the smaller the "absolute" value of critical stability number N_c. See Tables 1, 2 for the complete set of data.

Shown in Fig. 5 is a comparison of the failure mechanisms for *H/D* = 1, 5, and 10. The chosen case is of *B/D* = 1. On the left-handed side (LHS) of each colored contour plot, it is the shear dissipation. The non-zero shear dissipation (colored) indicated the potential shear band. The actual values of the contour are not important in such a perfectly plastic soil model, and therefore it is not shown in most research publications. On the right-handed side (RHS) of each plot is the final adaptive mesh. As discussed before, the adaptive mesh is also indicative of shear bands, which is the failure mechanism. Three distinct failure mechanisms are identified. The corner failure mode is mostly found in cases of shallow tunnels such as *H/D* = 1 (Fig. 5a). As the tunnel is located deeper, the wall and roof failure take place (see *H/D* = 5, Fig. 5b). Finally, for a deep tunnel such as *H/D* = 10 (Fig. 5c), the failure model is a combination of wall, roof, and base failures. It should be noted that the proposed failures in Fig. 5 are similar to the patterns of failure

Table 1 N_c results in collapse and blowout

Parameter		Collapse, N_c		Blowout, N_c	
H/D	*B/D*	LB	UB	LB	UB
1	1	1.947	1.962	− 1.911	− 1.981
	2	0.973	0.984	− 0.949	− 0.999
	3	0.627	0.635	− 0.619	− 0.642
	4	0.416	0.422	− 0.415	− 0.426
	5	0.292	0.295	− 0.290	− 0.298
	6	0.213	0.215	− 0.212	− 0.217
	8	0.124	0.127	− 0.129	− 0.128
	10	0.081	0.083	− 0.081	− 0.084
2	1	3.033	3.055	− 3.001	− 3.070
	2	2.101	2.117	− 1.928	− 1.976
	3	1.404	1.414	− 1.292	− 1.318
	4	0.975	0.981	− 0.968	− 0.987
	5	0.842	0.848	− 0.770	− 0.788
	6	0.691	0.696	− 0.624	− 0.637
	8	0.470	0.473	− 0.416	− 0.423
	10	0.331	0.334	− 0.291	− 0.295
3	1	3.610	3.640	− 3.598	− 3.668
	2	2.708	2.730	− 2.694	− 2.742
	3	1.950	1.962	− 1.940	− 1.970
	4	1.484	1.496	− 1.453	− 1.478
	5	1.171	1.179	− 1.162	− 1.183
	6	0.976	0.981	− 0.970	− 0.985
	8	0.727	0.730	− 0.719	− 0.733
	10	0.547	0.549	− 0.545	− 0.646
4	1	4.091	4.120	− 4.066	− 4.147
	2	3.205	3.250	− 3.197	− 3.265
	3	2.524	2.534	− 2.504	− 2.544
	4	1.951	1.961	− 1.939	− 1.968
	5	1.561	1.569	− 1.555	− 1.575
	6	1.305	1.307	− 1.294	− 1.312
	8	0.970	0.980	− 0.971	− 0.984
	10	0.778	0.783	− 0.772	− 0.786
5	1	4.493	4.524	− 4.452	− 4.551
	2	3.654	3.657	− 3.603	− 3.673
	3	2.970	2.991	− 2.922	− 3.003
	4	2.409	2.429	− 2.386	− 2.421
	5	1.952	1.963	− 1.943	− 1.966
	6	1.632	1.634	− 1.620	− 1.639
	8	1.221	1.225	− 1.215	− 1.229
	10	0.972	0.980	− 0.971	− 0.983

(*H/D* = 1–5)

Table 2 N_c results in collapse and blowout

Parameter		Collapse, N_c		Blowout, N_c	
H/D	*B/D*	LB	UB	LB	UB
6	1	4.836	4.873	− 4.786	− 4.898
	2	3.965	4.001	− 3.953	− 4.026
	3	3.322	3.343	− 3.310	− 3.363
	4	2.798	2.806	− 2.768	− 2.816
	5	2.312	2.324	− 2.308	− 2.339
	6	1.952	1.954	− 1.944	− 1.967
	8	1.454	1.465	− 1.456	− 1.475
	10	1.165	1.172	− 1.165	− 1.180
7	1	5.134	5.178	− 5.083	− 5.203
	2	4.280	4.315	− 4.240	− 4.336
	3	3.624	3.660	− 3.610	− 3.675
	4	3.118	3.133	− 3.090	− 3.144
	5	2.655	2.670	− 2.639	− 2.680
	6	2.264	2.274	− 2.254	− 2.281
	8	1.707	1.715	− 1.702	− 1.720
	10	1.367	1.372	− 1.363	− 1.376
8	1	5.397	5.441	− 5.316	− 5.467
	2	4.552	4.590	− 4.510	− 4.611
	3	3.906	3.936	− 3.871	− 3.953
	4	3.388	3.410	−3.350	− 3.424
	5	2.949	2.968	− 2.930	− 2.978
	6	2.554	2.568	− 2.541	− 2.576
	8	1.955	1.959	− 1.943	− 1.965
	10	1.562	1.568	− 1.558	− 1.573
9	1	5.608	5.669	− 5.549	− 5.696
	2	4.795	4.837	− 4.738	− 4.857
	3	4.153	4.185	− 4.097	− 4.203
	4	3.634	3.661	− 3.610	− 3.677
	5	3.200	3.223	− 3.184	− 3.234
	6	2.834	2.837	− 2.792	− 2.849
	8	2.189	2.199	− 2.177	− 2.206
	10	1.753	1.764	− 1.752	− 1.769
10	1	5.821	5.872	− 5.751	− 5.898
	2	5.018	5.062	− 4.979	− 5.083
	3	4.380	4.412	− 4.314	− 4.429
	4	3.862	3.871	− 3.812	− 3.906
	5	3.430	3.425	− 3.394	− 3.466
	6	3.052	3.075	− 3.031	− 3.086
	8	2.419	2.429	− 2.407	− 2.437
	10	1.950	1.959	− 1.945	− 1.965

(*H/D* = 6–10)

mechanisms suggested by Abbo et al. (2013) based on the rigid block mechanisms. The figures demonstrating three failures redrawn from those introduced by Abbo et al. (2013) are also shown in Fig. 5.

Figure 6 shows a comparison of failure mechanisms for *B/D* = 1, 5, 10. The depth ratio is chosen as shallow i.e., *H/D* = 1. Corner failures are recorded in all cases of *B/D*. Note the potential roof collapse near the symmetrical plane as the value of *B/D* is large (see Figs. 6b, c). On the other hand, as the tunnel is placed deeper, such as *H/D* = 7 (Fig. 7) and *H/D* = 10 (Fig. 8), the associated failure mechanisms are different. The larger the value of *B/D*, the more tendency

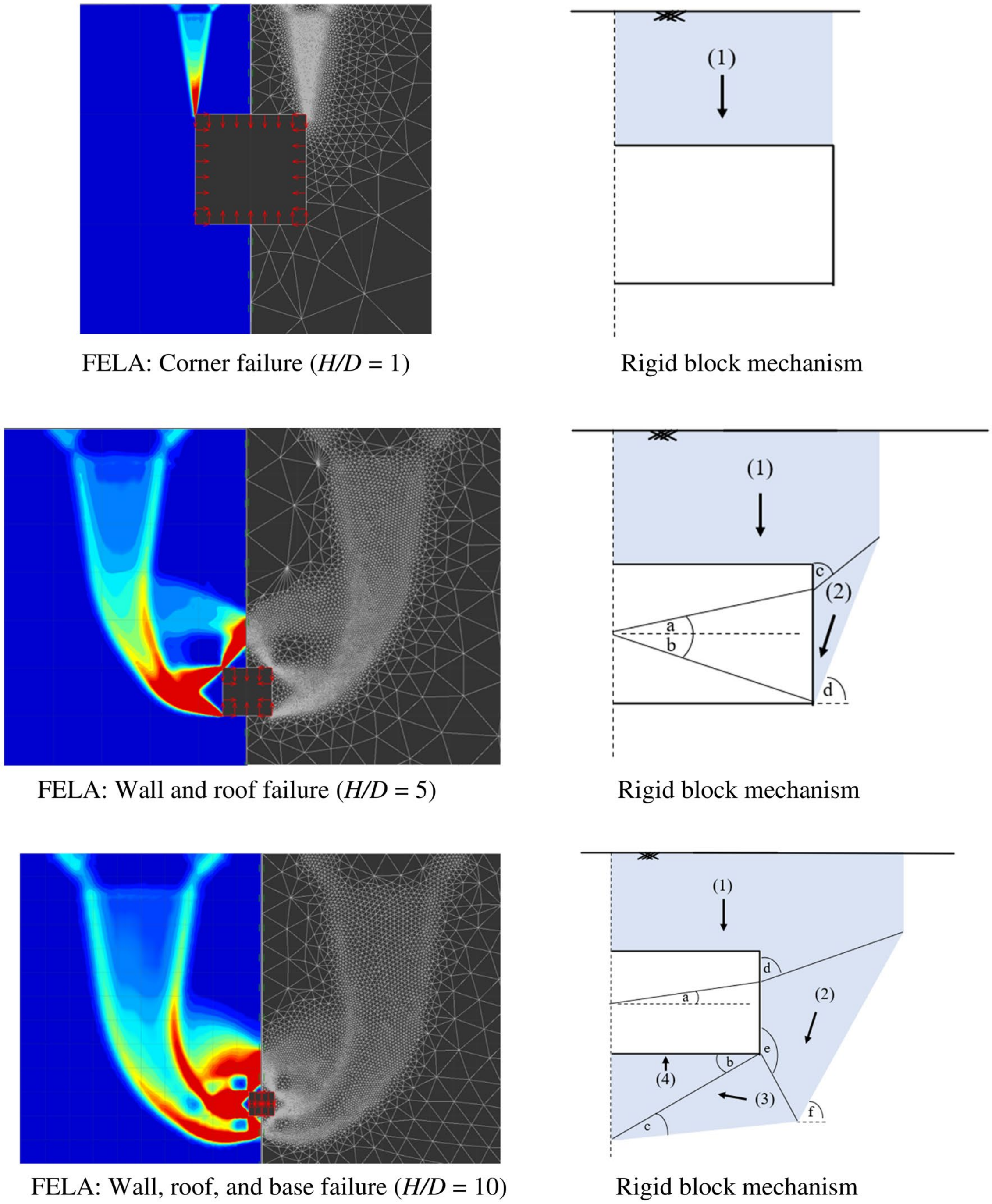

Fig. 5 Failure mechanisms (LHS) and final adaptive mesh (RHS) for $B/D=1$

it is for a corner failure and a local roof failure near the symmetrical plane. The smaller the value of *B/D*, the more tendency it is for a combined wall-roof-base failure. Having said that, the value of *H/D* also plays an important role in the resulting mechanisms. A summary of failure modes for all investigated cases ($H/D=1$–10 and $B/D=1$–10) is presented in Fig. 9. The identified three distinct zones are: (1). Zone I: Corner failure (CF); (2). Zone II: Wall and roof failure (WRF); and (3). Zone III: Wall, roof, and base failure (WRBF). This figure is useful for practical engineers to determine the likely associated ground failure extents.

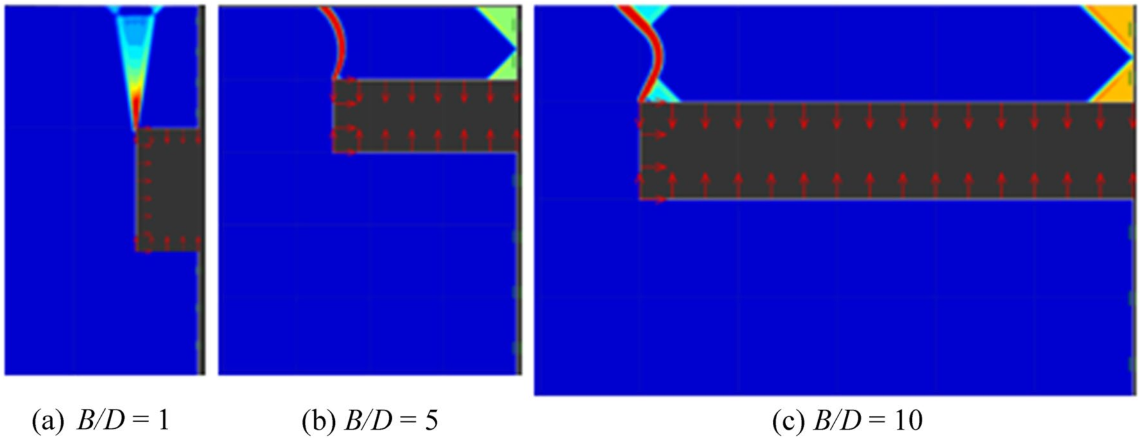

Fig. 6 Failure mechanisms for $H/D = 1$

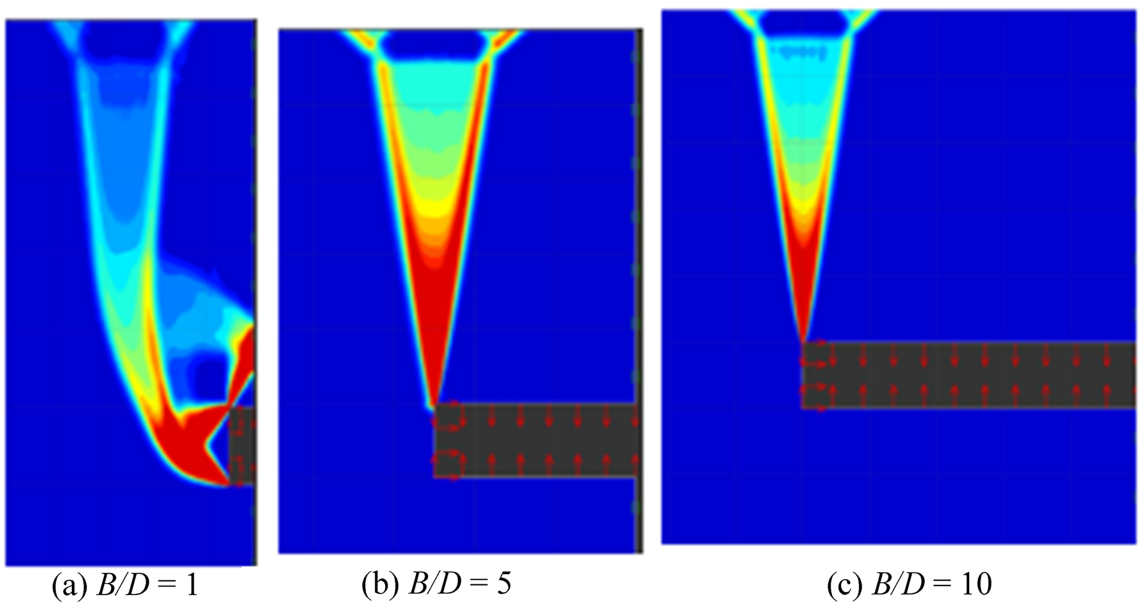

Fig. 7 Failure mechanisms for $H/D = 7$

The design equation and sensitivity analysis using MARS

MARS algorithm

In this study, MARS model–a machine learning method is used to develop a mathematical equation for predicting the stability number of the investigated tunnels and determining the relative importance of input variables. MARS model was firstly presented by Friedman (1991) for solving nonlinear regression problems based on a tree-based model of machine learning methods. MARS model has been widely applied in the geotechnical field (i.e., Lai et al. 2021; Qi et al. 2021; Zhang 2019; Zhang et al. 2019; 2021; Zheng et al. 2019; Ray et al. 2022; Zhou et al. 2021; Singh et al. 2022; Zeroual et al. 2022).

In general, the numerical process in MARS is to implement multiple linear regression models across the range of data. Instead of using nonlinear regression, MARS model is established in two steps. First, it splits the data into several groups and performs a linear regression model in each group. The regression lines with different slopes generated from linear regression models are connected with knots and mathematically expressed by basic functions (BFs), as

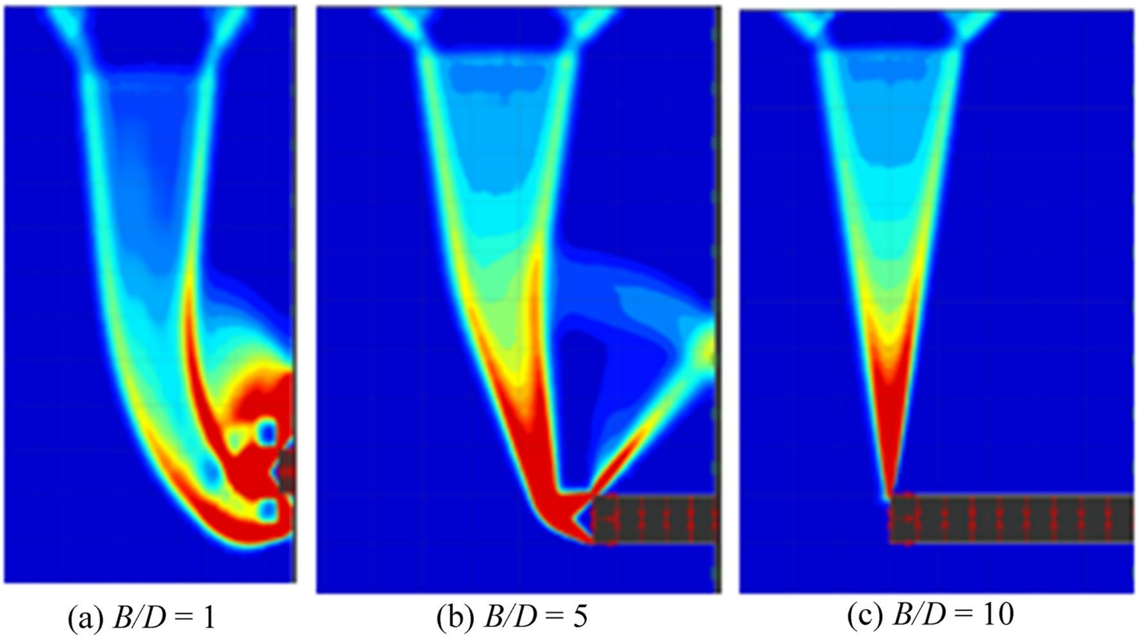

Fig. 8 Failure mechanisms for $H/D = 10$

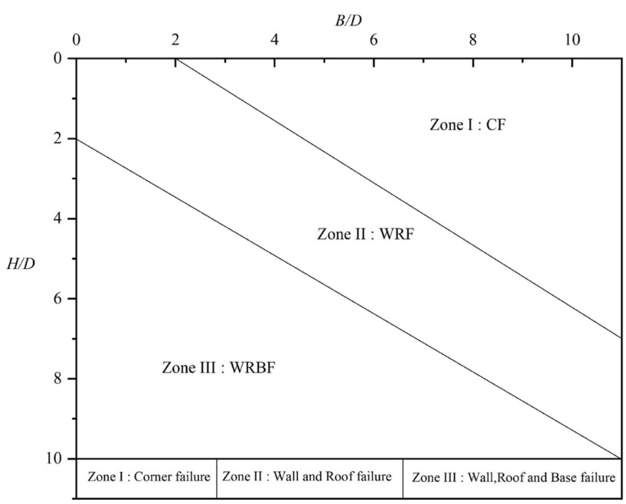

Fig. 9 Summary of all failure mechanisms

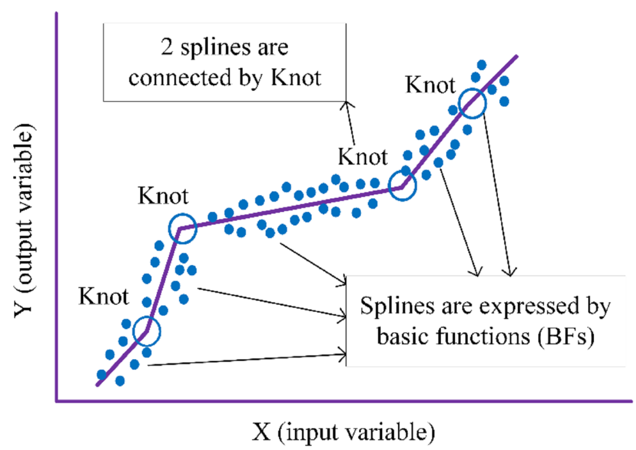

Fig. 10 Illustration of MARS model process

shown in Fig. 10. The locations of the knots are automatically searched by an optimal algorithm of MARS model. The basic function (BF) can be described as shown in Eq. (2).

$$BF = \max(0,\ x - t) = \begin{cases} x - t & \text{if } x > t \\ 0 & \text{otherwise} \end{cases} \tag{2}$$

where x is an input variable and t is a threshold value.

Second, it estimates a least-square model with its basis functions as independent variables by "pruning" algorithm based on Generalised Cross Validation (GCV) (like a tree-based model) to iteratively delete basis functions with the least fits. The definition of GCV is shown in Eq. (3). where $RMSE$ denotes the root mean square error for the training dataset, d denotes the penalty factor, R denotes the number of data points, and N denotes the number of basic functions.

$$GCV = \frac{RMSE}{\left[1 - (N - dN)/R\right]^2} \tag{3}$$

Based on the difference between GCV values between the previous and pruned models, MARS can examine the impact of each input parameter on the output parameter (Gan et al. 2014; Steinberg 1999). This progress can be simply represented by Eq. (4)

$$RII(i) = \frac{\Delta g(i)}{\max\{\Delta g(i), \Delta g(2), \Delta g(3), \ldots, \Delta g(n)\}} \quad (4)$$

where Δg is the difference in *GCV* between the previous and pruned models, i^{th} parameter denotes the removed parameter. The larger the Δg, the more impact the removed parameter is.

To build a formula between the input and output variables, the MARS model combines all basic functions (BFs), as shown in Eq. (5), where a_0 denotes a constant, N denotes the number of BFs, g_n denotes the n^{th} BF, a_n denote the n^{th} coefficient of g_n.

$$f(x) = a_0 + \sum_{n=1}^{N} a_n g_n(X) \quad (5)$$

Similar to the concept as in most numerical analyses, by increasing the number of basic functions (i.e., increasing the number of splitting data groups shown in Fig. 10), it would significantly improve the performance of MARS models.

MARS modelling and results

In this study, numerical results of the stability numbers N_c and the input variables of *H/B* and *D/B* (see Tables 1, 2) are used as the artificial data sets. There are four MARS models to analyze, namely for cases of collapse (UB, LB) and blowout (UB, LB). The optimal MARS models are firstly selected by considering the effects of the number of basic functions on two criteria of statistical analyses. They are the coefficient of determination (R^2 value) and Mean Squared Error (MSE), as shown in Fig. 11. It is obtained that the R^2 value may increase and MSE decreases dramatically by increasing of number of BFs varied from 5 to 25 for all cases. When the number of BFs is larger than 25, the change in R^2 value and MSE are insignificant and almost stable when the number BFs reaches 35 for all cases. It can, therefore, be concluded that the MARS models can be used for determining

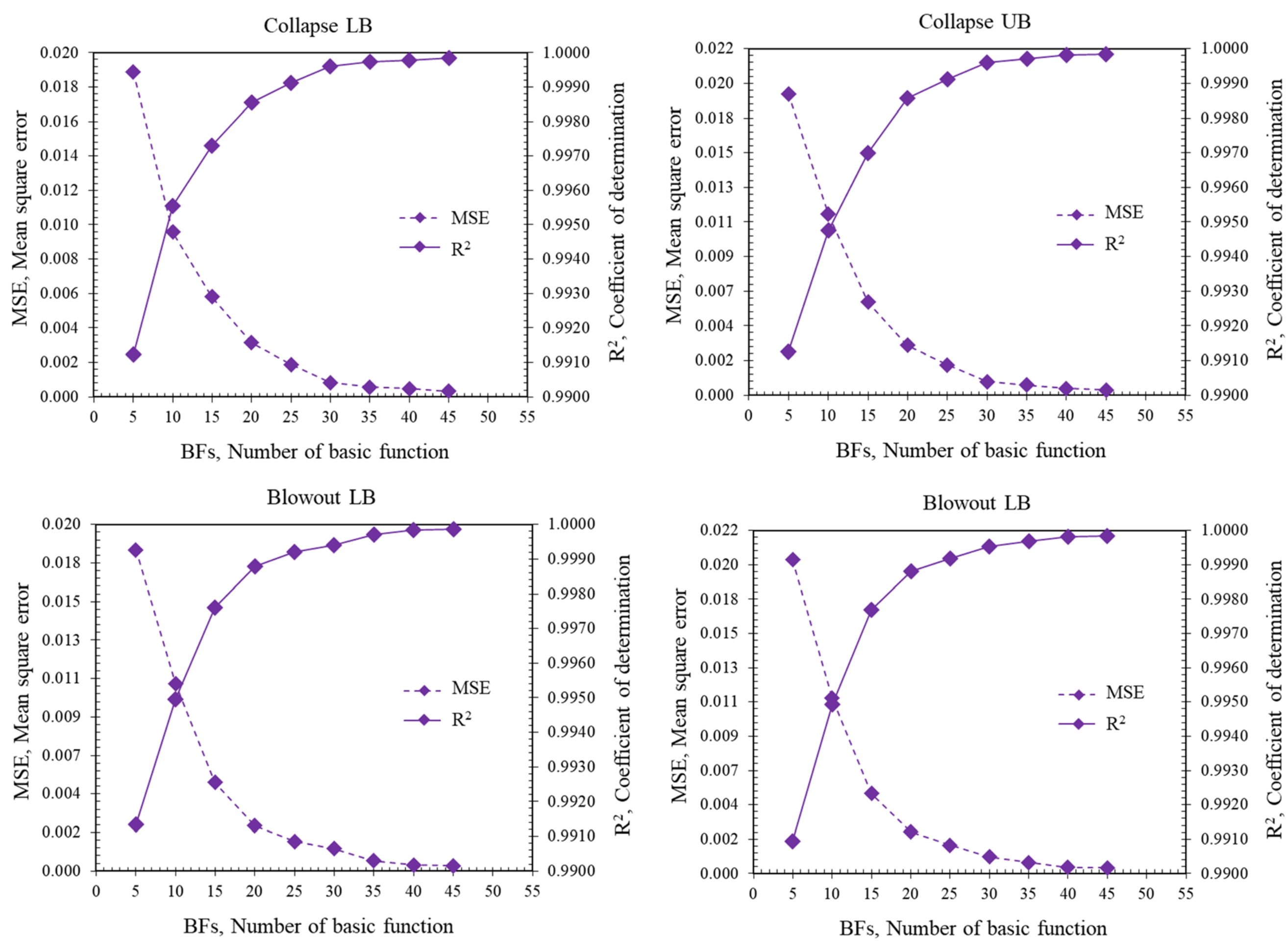

Fig. 11 Effect of number basic functions on R^2 and mean square error (*MSE*)

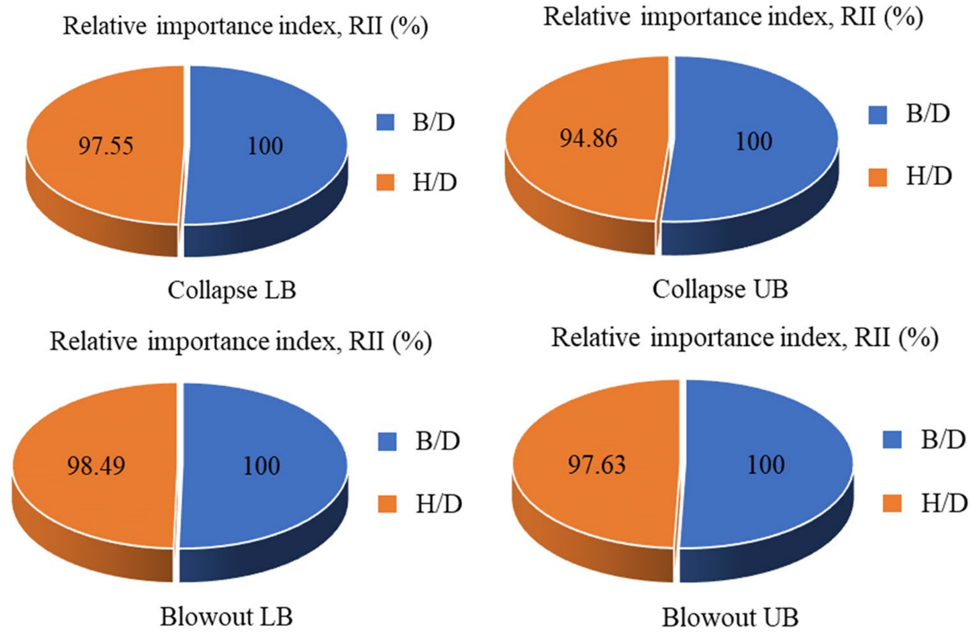

Fig. 12 Relative Importance Index (RII) of investigated input parameters

Table 3 Basic functions and the proposed equation for the determination of N_c (Collapse LB)

BF	Equation	BF	Equation
BF1	max [0, (B/D – 4)]	BF15	max [0, (H/D – 3)] × BF12
BF2	max [0, (4 – B/D)]	BF18	max [0, (4 – H/D)] × BF9
BF3	max [0, (H/D – 4)]	BF19	max (0, (H/D – 2)]
BF4	max [0, (4 – H/D)]	BF22	max [0, (4 – B/D)] × BF19
BF5	max [0, (H/D – 4)] × BF1	BF23	max [0, (B/D – 3)]
BF6	max [0, (4 – H/D)] × BF1	BF24	max [0, (3 – B/D)]
BF7	max [0, (H/D – 4)] × BF2	BF25	max [0, (B/D – 8)] × BF19
BF8	max [0, (4 – H/D)] × BF2	BF27	max [0, (H/D – 7)] × BF24
BF9	max [0, (B/D – 2)]	BF28	max [0, (7 – H/D)] × BF24
BF11	max [0, (B/D – 6)]	BF29	max [0, (H/D – 5)] × BF12
BF12	max [0, (6 – B/D)]	BF31	max [0, (B/D – 5)]
BF14	max (0, (7 – H/D)] × BF12	BF33	max [0, (H/D – 8)]

$N_c = 1.9911 - 0.718887 \times BF1 + 1.23918 \times BF2 + 0.472754 \times BF3 - 0.719808 \times BF4 - 0.0325413 \times BF5 - 0.0604259 \times BF6 + 0.17425 \times BF7 - 0.101537 \times BF8 + 0.171618 \times BF9 + 0.24606 \times BF11 - 0.03598 \times BF14 - 0.0131068 \times BF15 + 0.10195 \times BF18 - 0.0990932 \times BF19 - 0.168136 \times BF22 + 0.0669792 \times BF23 + 0.0168681 \times BF25 + 0.0417739 \times BF27 + 0.0307377 \times BF28 - 0.0295754 \times BF29 + 0.0731142 \times BF31 - 0.0369426 \times BF33$

Table 4 Basic functions and the proposed equation for the determination of N_c (Collapse UB)

BF	Equation	BF	Equation
BF1	max [0, (B/D – 4)]	BF15	max [0, (H/D – 3)] × BF12
BF2	max [0, (4 – B/D)]	BF18	max [0, (4 – H/D)] × BF9
BF3	max [0, (H/D – 4)]	BF19	max [0, (H/D – 2)]
BF4	max [0, (4 – H/D)]	BF22	max [0, (4 – B/D)] × BF19
BF5	max [0, (H/D – 4)] × BF1	BF24	max [0, (3 – B/D)]
BF6	max [0, (4 – H/D)] × BF1	BF25	max [0, (B/D – 8)] × BF19
BF7	max [0, (H/D – 4)] × BF2	BF27	max [0, (H/D – 7)] × BF24
BF8	max [0, (4 – H/D)] × BF2	BF28	max [0, (7 – H/D)] × BF24
BF9	max [0, (B/D – 2)]	BF29	max [0, (H/D – 5)] × BF12
BF11	max [0, (B/D – 6)]	BF31	max [0, (B/D – 5)]
BF12	max [0, (6 – B/D)]	BF33	max [0, (H/D – 8)]
BF14	max [0, (7 – H/D)] × BF12		

$N_c = 2.035 - 0.702954 \times BF1 + 1.23278 \times BF2 + 0.475089 \times BF3 - 0.684739 \times BF4 - 0.032949 \times BF5 - 0.0475025 \times BF6 + 0.173106 \times BF7 - 0.114032 \times BF8 + 0.204152 \times BF9 + 0.272293 \times BF11 - 0.0410779 \times BF14 - 0.0179609 \times BF15 + 0.0875601 \times BF18 - 0.098312 \times BF19 - 0.161922 \times BF22 + 0.0167148 \times BF25 + 0.0483571 \times BF27 + 0.0432518 \times BF28 - 0.0286598 \times BF29 + 0.0671558 \times BF31 - 0.0379595 \times BF33$

the relative importance of input variables (*H/B*, *D/B*) on the stability number with the use of 35 BFs. It can also be used to build a correlation formula between input variables and the stability number for all cases of collapse (UB, LB) and blowout (UB, LB).

Presented in Fig. 12 are the results of relative important assessments through the use of the relative importance index (*RII*), as the definition in Eq. (4). A *RII* value of 100% is considered as the most important variable in the determination of the critical stability number N_c, and this is true for the width ratio *B/D*. For the depth ratio *H/D*, the *RIIs* are in the range of 94.86–98.49%. Though these *RIIs* are less than 100% by a small amount, the effect of *H/D* on the critical stability number N_c is also regarded as significant.

The correlation equations between the input variables and the critical stability number N_c with their BFs are presented in Tables 3, 4, 5, 6, respectively, for (Collapse, LB),

Table 5 Basic functions and the proposed equation for the determination of N_c (Blowout LB)

BF	Equation	BF	Equation
BF1	max [0, (B/D – 4)]	BF19	max [0, (B/D – 8)] × BF3
BF2	max [0, (4 – B/D)]	BF21	max [0, (H/D – 6)]
BF3	max [0, (H/D – 4)]	BF22	max [0, (6 – H/D)]
BF4	max [0, (4 – H/D)]	BF23	max [0, (B/D – 3)] × BF22
BF6	max [0, (4 – H/D)] × BF1	BF24	max [0, (3 – B/D)] × BF22
BF7	max [0, (H/D – 4)] × BF2	BF25	max [0, (B/D – 3)] × BF3
BF9	max [0, (B/D – 2)]	BF27	max [0, (B/D – 8)]
BF1	max [0, (B/D – 6)]	BF28	max [0, (8 – B/D)]
BF12	max [0, (6 – B/D)]	BF29	max [0, (H/D – 2)]
BF13	max [0, (H/D – 7)] × BF12	BF32	max [0, (4 – B/D)] × BF29
BF14	max [0, (7 – H/D)] × BF12	BF33	max [0, (H/D – 8)] × BF28
BF15	max [0, (H/D – 3)] × BF12	BF34	max [0, (8 – H/D)] × BF28
BF18	max [0, (4 – H/D)] × BF9		

N_c = −2.53932 + 0.853413 × BF1 – 1.37941 × BF2 – 0.23592 × BF3 + 0.587962 × BF4 + 0.15796 × BF6 – 0.0889785 × BF7 – 0.170739 × BF9 – 0.292476 × BF11 – 0.032003 × BF13 + 0.0368904 × BF14 + 0.0401248 × BF15 – 0.142922 × BF18 + 0.0450297 × BF19 + 0.128742 × BF21 – 0.0208616 × BF23 – 0.0279392 × BF24 – 0.0259664 × BF25 – 0.273361 × BF27 + 0.124927 × BF32 – 0.0350765 × BF33 + 0.0436685 × BF34

Table 6 Basic functions and the proposed equation for the determination of N_c (Blowout UB)

BF	Equation	BF	Equation
BF1	max [0, (B/D – 4)]	BF19	max [0, (B/D – 8)] × BF3
BF2	max [0, (4 – B/D)]	BF21	max [0, (H/D – 6)]
BF3	max [0, (H/D – 4)]	BF22	max [0, (6 – H/D)]
BF4	max [0, (4 – H/D)]	BF23	max [0, (B/D – 3)] × BF22
BF6	max [0, (4 – H/D)] × BF1	BF24	max [0, (3 – B/D)] × BF22
BF7	max [0, (H/D – 4)] × BF2	BF25	max [0, (B/D – 8)]
BF9	max [0, (B/D – 2)]	BF26	max [0, (8 – B/D)]
BF11	max [0, (B/D – 6)]	BF27	max [0, (H/D – 2)]
BF12	max [0, (6 – B/D)]	BF30	max (0, (4 – B/D)] × BF27
BF13	max [0, (H/D – 7)] × BF12	BF31	max [0, (B/D – 3)] × BF3
BF14	max [0, (7 – H/D)] × BF12	BF33	max [0, (H/D – 8)] × BF26
BF15	max [0, (H/D – 3)] × BF12	BF34	max [0, (8 – H/D)] × BF26
BF18	max [0, (4 – H/D)] × BF9		

N_c = 1.9911 – 0.718887 × BF1 + 1.23918 × BF2 + 0.472754 × BF3 – 0.719808 × BF4 – 0.0325413 × BF5 – 0.0604259 × BF6 + 0.17425 × BF7 – 0.101537 × BF8 + 0.171618 × BF9 + 0.24606 × BF11 – 0.03598 × BF14 – 0.0131068 × BF15 + 0.10195 × BF18 – 0.0990932 × BF19 – 0.168136 × BF22 + 0.0669792 × BF23 + 0.0168681 × BF25 + 0.0417739 × BF27 + 0.0307377 × BF28 – 0.0295754 × BF29 + 0.0731142 × BF31 – 0.0369426 × BF33

(Collapse, UB), (Blowout, LB), and (Blowout, UB). The four equations are shown in Eqs. (6, 7, 8, 9).

$$\begin{aligned} N^{LB}_{\text{c - collapse}} = {} & 1.9911 - 0.718887 \times \text{BF1} + 1.23918 \times \text{BF2} \\ & + 0.472754 \times \text{BF3} - 0.719808 \times \text{BF4} - 0.0325413 \\ & \times \text{BF5} - 0.0604259 \times \text{BF6} + 0.17425 \times \text{BF7} \\ & - 0.101537 \times \text{BF8} + 0.171618 \times \text{BF9} + 0.24606 \\ & \times \text{BF11} - 0.03598 \times \text{BF14} - 0.0131068 \times \text{BF15} \\ & + 0.10195 \times \text{BF18} - 0.0990932 \times \text{BF19} - 0.168136 \\ & \times \text{BF22} + 0.0669792 \times \text{BF23} + 0.0168681 \times \text{BF25} \\ & + 0.0417739 \times \text{BF27} + 0.0307377 \times \text{BF28} - 0.0295754 \\ & \times \text{BF29} + 0.0731142 \times \text{BF31} - 0.0369426 \times \text{BF33} \end{aligned} \tag{6}$$

$$\begin{aligned} N^{UB}_{\text{c - collapse}} = {} & 2.035 - 0.702954 \times \text{BF1} + 1.23278 \\ & \times \text{BF2} + 0.475089 \times \text{BF3} - 0.684739 \\ & \times \text{BF4} - 0.032949 \times \text{BF5} - 0.0475025 \\ & \times \text{BF6} + 0.173106 \times \text{BF7} - 0.114032 \\ & \times \text{BF8} + 0.204152 \times \text{BF9} + 0.272293 \\ & \times \text{BF11} - 0.0410779 \times \text{BF14} - 0.0179609 \\ & \times \text{BF15} + 0.0875601 \times \text{BF18} - 0.098312 \\ & \times \text{BF19} - 0.161922 \times \text{BF22} + 0.0167148 \\ & \times \text{BF25} + 0.0483571 \times \text{BF27} + 0.0432518 \\ & \times \text{BF28} - 0.0286598 \times \text{BF29} + 0.0671558 \\ & \times \text{BF31} - 0.0379595 \times \text{BF33} \end{aligned} \tag{7}$$

$$\begin{aligned} N^{LB}_{\text{c - blowout}} = {} & -2.53932 + 0.853413 \times \text{BF1} - 1.37941 \\ & \times \text{BF2} - 0.23592 \times \text{BF3} + 0.587962 \\ & \times \text{BF4} + 0.15796 \times \text{BF6} - 0.0889785 \\ & \times \text{BF7} - 0.170739 \times \text{BF9} - 0.292476 \\ & \times \text{BF11} - 0.032003 \times \text{BF13} + 0.0368904 \\ & \times \text{BF14} + 0.0401248 \times \text{BF15} - 0.142922 \\ & \times \text{BF18} + 0.0450297 \times \text{BF19} + 0.128742 \\ & \times \text{BF21} - 0.0208616 \times \text{BF23} - 0.0279392 \\ & \times \text{BF24} - 0.0259664 \times \text{BF25} - 0.273361 \\ & \times \text{BF27} + 0.124927 \times \text{BF32} - 0.0350765 \\ & \times \text{BF33} + 0.0436685 \times \text{BF34} \end{aligned} \tag{8}$$

$$\begin{aligned} N^{UB}_{\text{c - blowout}} = {} & 1.9911 - 0.718887 \times \text{BF1} + 1.23918 \\ & \times \text{BF2} + 0.472754 \times \text{BF3} - 0.719808 \\ & \times \text{BF4} - 0.0325413 \times \text{BF5} - 0.0604259 \\ & \times \text{BF6} + 0.17425 \times \text{BF7} - 0.101537 \\ & \times \text{BF8} + 0.171618 \times \text{BF9} + 0.24606 \\ & \times \text{BF11} - 0.03598 \times \text{BF14} - 0.0131068 \\ & \times \text{BF15} + 0.10195 \times \text{BF18} - 0.0990932 \\ & \times \text{BF19} - 0.168136 \times \text{BF22} + 0.0669792 \\ & \times \text{BF23} + 0.0168681 \times \text{BF25} + 0.0417739 \\ & \times \text{BF27} + 0.0307377 \times \text{BF28} - 0.0295754 \\ & \times \text{BF29} + 0.0731142 \times \text{BF31} - 0.0369426 \times \text{BF33} \end{aligned} \tag{9}$$

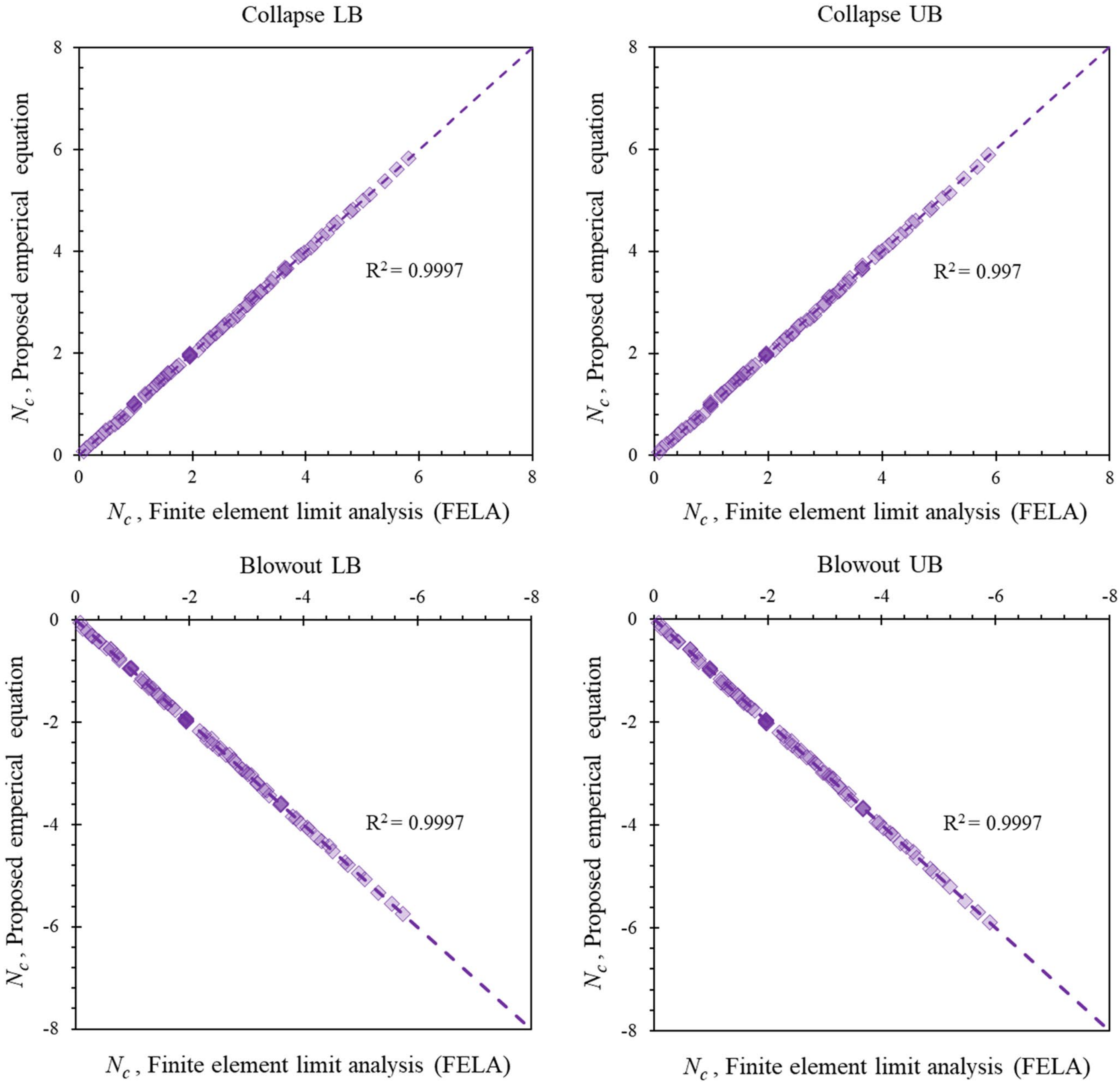

Fig. 13 Comparison of results– the finite element analysis and the proposed equation

The accuracy of the Eqs. (6, 7, 8, 9) can be demonstrated by using Fig. 13, where a comparison between the values of stability numbers is made between the proposed correlation equation and the FELA results. Numerical results have shown a good agreement between the two solutions with a very high R^2 of 99.97%. It can, therefore, be concluded that the proposed correlation equations can be used effectively in design practices.

Factor of safety

A series of undrained stability studies of underground tunneling on the relationship between *FoS* and *N* was performed by Shiau and Al-Asadi (2018; 2020a, b; 2021). It was concluded by the authors that the relationship between *FoS* and the "designed" *N* is in a hyperbolic form where *FoS* and the "designed" *N* are the vertical and horizontal asymptote,

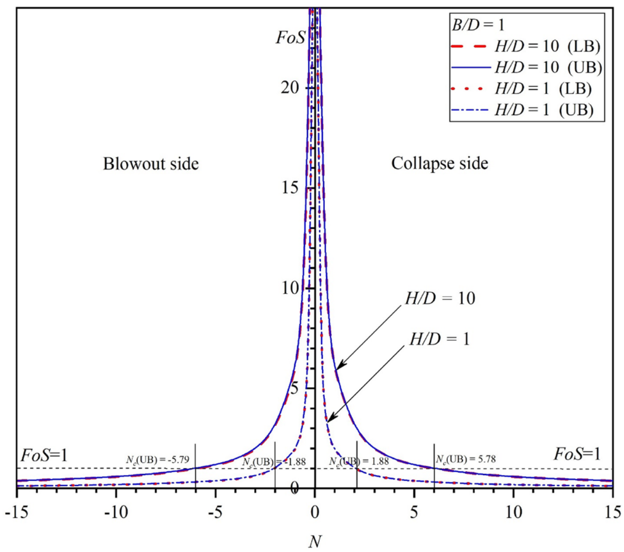

Fig. 14 *FoS* versus *N* (*B/D* = 1, *H/D* = 1 and 10)

respectively. The equation proposed by the authors is shown in Eq. (10), where it implies that $FoS = 1$ when the "designed" N is equal to the critical N_c.

$$FoS = \frac{N_c}{N} \tag{10}$$

Using Eq. (10), while considering the combined effect of *B/D* and *H/D* on the "designed" stability number *N*, the factor safety *FoS* for the rectangular tunnel can be calculated using Eqs. (11) and (12) for the collapse scenarios. On the other hand, Eqs. (13) and (14) can be used for evaluating the blowout *FoS*.

$$FoS^{LB}_{\text{- collapse}} = (N^{LB}_{\text{c - collapse}})/N \ \text{(for collapse, lower bound)} \tag{11}$$

$$FoS^{UB}_{\text{- collapse}} = (N^{UB}_{\text{c - collapse}})/N \ \text{(for collapse, upper bound)} \tag{12}$$

$$FoS^{LB}_{\text{- blowout}} = (N^{LB}_{\text{c - blowout}})/N \ \text{(for blowout, lower bound)} \tag{13}$$

$$FoS^{UB}_{\text{- blowout}} = (N^{UB}_{\text{c - blowout}})/N \ \text{(for blowout, upper bound)} \tag{14}$$

where $(N^{LB}_{\text{c - collapse}})$, $(N^{UB}_{\text{c - collapse}})$, $(N^{LB}_{\text{c - blowout}})$, and $(N^{UB}_{\text{c - blowout}})$ are the equations developed by the earlier MARS models. See Eqs. (6, 7, 8, 9).

Using Eqs. (11, 12, 13, 14), a comprehensive set of *FoS* data is presented in Fig. 14 showing the asymptotic relationship between *N* and *FoS*. The presented data are for both upper and lower bounds of (*B/D* = 1, *H/D* = 1, and 10). In addition, results for both the collapse (i.e., positive *N*) and the blowout (i.e., negative *N*) conditions are also presented in the figure. By drawing a horizontal line through $FoS = 1$, the four intersected points represent the respective values of N_c, where the corresponding $FoS = 1$. The greater the absolute value of "designed" *N*, the less the value of *FoS* in both collapse and blowout scenarios. Indeed, the results in Fig. 14 and Eq. (10) make perfect sense for the current undrained stability analysis, in that S_u is the only strength parameter considered in the analysis. For drained analysis with non-zero soil frictional angle, the solutions are completely

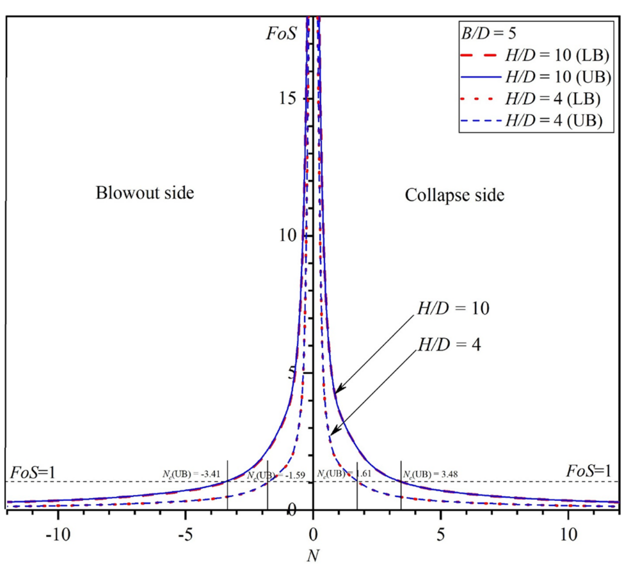

Fig. 15 *FoS* versus *N* (*B/D* = 5, *H/D* = 4 and 10)

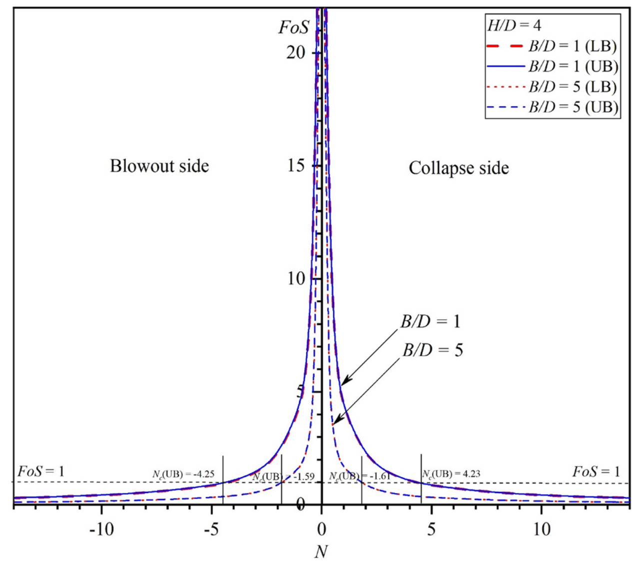

Fig. 16 *FoS* versus *N* (*H/D* = 4, *B/D* = 1 and 5)

different and yet highly nonlinear, and the three stability factors approach is advocated (Shiau and Al-Asadi 2021).

Following the presentation in Fig. 14, the selected data for Fig. 15 are for ($B/D=5$, $H/D=4$ and 10). The same observation and discussion can be drawn as in Fig. 14. On the other hand, shown in Fig. 16 are solutions for a fixed depth ratio ($H/D=4$) and two width ratios ($B/D=1$ and 5). It should be noted that the smaller the value of *B/D*, the larger the *FoS*. All other observations are the same as in Fig. 14.

Conclusion

This paper has successfully studied the stability of wide rectangular tunnels for railway engineering applications. The relationship between the critical stability number N_c, the factor of safety *FoS*, and the designed stability number *N* were presented under both collapse and blowout conditions. Using upper and lower bound limit analysis with finite elements and mathematical programming, rigorous stability solutions were produced for practical uses with great confidence. Together with the use of the machine learning method MARS, both the relative importance index (RII) and the *FoS* design equations were also developed for practical uses. The following conclusions are drawn based on the current study.

1. The use of dimensionless critical stability number N_c for the stability evaluation of wide rectangular tunnels in cohesive soil is a feasible and practical approach. An increase in *H/D* causes an increase in N_c. On the other hand, an increase in *B/D* results in a decrease in N_c.
2. The relationship between *FoS* and the "designed" *N* is in a hyperbolic form where *FoS* and the "designed" *N* are the vertical and horizontal asymptote, respectively. The equation of ($FoS=N_c/N$) is valid, and it indicates that $FoS=1$ when the "designed" *N* is equal to the critical N_c.
3. The study of associated failure mechanisms led to a conclusion of three distinct patterns of failures, namely the corner, the wall-roof, and the wall-roof-base failure. The current adaptive meshing technique is powerful as the resulting adaptive mesh resembles the non-zero shear dissipation contour plot (i.e., the failure mechanism). The findings are useful for practical engineers to determine the likely associated ground failure extents.
4. The MARS machine learning models showed that the width ratio *B/D* is more influential than the depth ratio *H/D* on the undrained stability number of wide rectangular tunnels in cohesive soils. The well-evaluated MARS-based design equations with $R^2=99.97\%$ are proposed for predicting the limit state solutions of rectangular tunnel stability. It can be a useful tool for practical engineering practitioners.
5. Future work can be directed to studies of deep and wide rectangular tunnels in rocks and drained c- ϕ for longwall mining applications. The study of 3D local failure mechanisms considering geometric arching effects may further improve the understanding of the problem using more realistic 3D geometry.

Acknowledgements We acknowledge Ho Chi Minh City University of Technology (HCMUT), VNU-HCM for supporting this study.

Funding This study was financially supported by Office of the Permanent Secretary, Ministry of Higher Education, Science, Research and Innovation under Research Grant for New Scholar (RGNS 64-134); and by the Thailand Research Fund (TRF) under Grant (RTA6280012).

Data availability All data, models, or code that support the findings of this study are available from the corresponding author upon reasonable request.

Declarations

Conflict of interest The authors declare no conflict of interest.

References

Abbo AJ, Wilson DW, Sloan SW, Lyamin AV (2013) Undrained stability of wide rectangular tunnels. Comput Geotech 53:46–59

Arjenaki MO (2022) Predicting the amount of face seepage during the excavation of the mechanized tunnel, using numerical and analytical methods. Model Earth Syst Environ 8:2889–2896

Assadi A, Sloan SW (1991) Undrained stability of shallow square tunnel. J Geotechnical Eng 117(8):1152–1173

Atkinson JH, Potts DM (1977) Stability of a shallow circular tunnel in cohesionless soil. Geotechnique 27(2):203–215. https://doi.org/10.1680/geot.1977.27.2.203

Broms BB, Bennermark H (1967) Stability of clay at vertical openings. J Soil Mech Found Division Proc Am Soc Civ Eng 93:71–94

Chambon P, Corté JF (1994) Shallow tunnels in cohesionless soil: stability of tunnel face. J Geotech Eng 120(7):1148–1165. https://doi.org/10.1061/(ASCE)0733-9410(1994)120:7(1148)

Chen X, Ma B, Najafi M, Zhang P (2021) Long rectangular box jacking project: a case study. Underground Space 6(2):101–125

Dutta P, Bhattacharya P (2019) Stability of rectangular tunnel in cohesionless soils. Int J Geotech Eng. https://doi.org/10.1080/19386362.2019.1592874

Friedman JH (1991) Multivariate adaptive regression splines. Ann Stat 19(1):1–67

Gan Y, Duan Q, Gong W, Tong C, Sun Y, Chu W, Di Z (2014) A comprehensive evaluation of various sensitivity analysis methods: a case study with a hydrological model. Environ Model Softw 51:269–285

Jamshidi A (2018) Prediction of TBM penetration rate from brittleness indexes using multiple regression analysis. Model Earth Syst Environ 4:383–394

Krabbenhoft K, Lyamin A, Krabbenhoft J. (2015) Optum Computational Engineering (Optum G2). Available online: www.optumce.com Accessed 1 Sep 2019

Lai F, Zhang N, Liu S, Sun Y, Li Y (2021) Ground movements induced by installation of twin large diameter deeply-buried caissons: 3D numerical modeling. Acta Geotech 16:2933–2961

Leca E, Dormieux L (1990) Upper and lower bound solutions for the face stability of shallow circular tunnels in frictional material. Geotechnique 40(4):581–606. https://doi.org/10.1680/geot.1990.40.4.581

Mollon G, Dias D, Soubra AH (2009) Probabilistic analysis and design of circular tunnels against face stability. Int J Geomech 9(6):237–249

Mollon G, Dias D, Soubra AH (2010) Face stability analysis of circular tunnels driven by a pressurized shield. J Geoteh Geoenviron Eng 136(1):215–229

Mühlhaus HB (1985) Lower bound solutions for circular tunnels in two and three dimensions. Rock Mech Rock Eng 18(1):37–52. https://doi.org/10.1007/BF01020414

Qi X, Wang H, Pan X, Chu J, Chiam K (2021) Prediction of interfaces of geological formations using the multivariate adaptive regression spline method. Underground Space 6(3):252–266

Ray R, Choudhary SS, Roy LB (2022) Reliability analysis of soil slope stability using MARS, GPR and FN soft computing techniques. Model Earth Syst Environ 8:2347–2357

Sahoo JP, Kumar J (2014) Stability of a circular tunnel in presence of pseudostatic seismic body forces. Tunn Undergr Space Technol 42:264–276

Shiau J, Al-Asadi F. (2021) Revisiting circular tunnel stability using broms and bennermarks original stability number. Int J Geomech, ASCE, 21(5)

Shiau J, Al-Asadi F (2018) Revisiting Broms and Bennermarks' original stability number for tunnel headings. Géotech Lett 8(4):310–315

Shiau J, Al-Asadi F (2020a) Stability analysis of twin circular tunnels using shear strength reduction method. Géotech Lett 10(2):311–319

Shiau J, Al-Asadi F (2020b) Three-dimensional heading stability of twin circular tunnels. Geotech Geol Eng 38:2973–2988

Shiau J, Keawsawasvong S (2022) Producing undrained stability factors for various tunnel shapes. Int J Geomech, ASCE 22(8):06022017

Shiau J, Chudal B, Mahalingasivam K, Keawsawasvong S (2021a) Pipeline burst-related ground stability in blowout condition. Transp Geotech 29:100587

Shiau J, Lee J-S, Al-Asadi F (2021b) Three-dimensional stability analysis of active and passive trapdoors. Tunn Undergr Space Technol 107:103635

Shiau J, Chudal B, Keawsawasvong S (2022a) Three-dimensional sinkhole stability of spherical cavity. Acta Geotech 17:3947–3958

Shiau J, Keawsawasvong S, Lee J (2022b) Three-dimensional stability investigation of trapdoors in collapse and blowout conditions. Int J Geomech, ASCE 22(4):04022007

Shiau JS, Lyamin AV, Sloan, SW. (2004) Rigorous solution of classical lateral earth pressures. 6th Young Geotechnical Professionals Conference, Gold Coast, Australia. 162–167

Shiau JS, Lyamin AV, Sloan SW. (2006) Application of pseudo-static limit analysis in geotechnical earthquake design. In: 6th European Conference on Numerical Methods in Geotechnical Engineering, 6–8, Graz, Austria

Singh P, Bardhan A, Han F et al. (2022) A critical review of conventional and soft computing methods for slope stability analysis. Model Earth Syst Environ

Sloan SW, Assadi A (1993) Stability of shallow tunnels in soft ground. In: Holsby GT, Schofield AN (eds) Predictive soil mechanics. Thomas Telford, London, pp 644–663

Sloan SW (2013) Geotechnical stability analysis. Géotechnique 63(7):531–572

Soleiman Dehkordi M, Lazemi HA, SaeedModaghegh HR (2019) Estimation of the drop modulus using the brittleness index of intact rock and geological strength index of rock mass, case studies: Nosoud and Zagros tunnels in Iran. Model Earth Syst Environ 5:479–492

Steinberg D, Colla PL, Martin K (1999) MARS user guide. Salford Systems, San Diego CA

Vinod M, Khabbaz H (2019) Comparison of rectangular and circular bored twin tunnels in weak ground. Underground Space 4(4):328–339

Wilson DW, Abbo AJ, Sloan SW, Lyamin AV (2011) Undrained stability of a circular tunnel where the shear strength increases linearly with depth. Can Geotech J 48:1328–1342. https://doi.org/10.1139/t11-041

Wilson DW, Abbo AJ, Sloan SW, Lyamin AV (2013) Undrained stability of a square tunnel where the shear strength increases linearly with depth. Comput Geotech 49:314–325. https://doi.org/10.1016/j.compgeo.2012.09.005

Yamamoto K, Lyamin AV, Wilson DW, Sloan SW, Abbo AJ (2011) Stability of a single tunnel in cohesive-frictional soil subjected to surcharge loading. Can Geotech J 48:1841–1854. https://doi.org/10.1139/t11-078

Yang F, Zhang J, Yang J, Zhao L, Zheng X (2015) Stability analysis of unlined elliptical tunnel using finite element upper-bound method with rigid translatory moving elements. Tunn Undergr Space Technol 50:13–22. https://doi.org/10.1016/j.tust.2015.06.005

Yatsumoto H, Mitsuyoshi Y, Sawamura Y, Kimura M (2019) Evaluation of seismic behavior of box culvert buried in the ground through centrifuge model tests and numerical analysis. Underground Space 4(2):147–167

Yodsomjai W, Keawsawasvong S, Senjuntichai T (2021) Undrained stability of unsupported conical slopes in anisotropic clays based on anisotropic undrained shear failure criterion. Transp Infrastructure Geotechnol 8(4):557–568

Zeroual A, Fourar A, Merrouchi F et al (2022) Modeling and prediction of earthquake-related settlement in embankment dams using nonlinear tools. Model Earth Syst Environ 8:1949–1962

Zhang W (2019) MARS applications in geotechnical engineering systems. Springer, Beijing

Zhang J, Yang J, Yang F, Zhang X, Zheng X (2017) Upper bound solution for stability number of elliptical tunnel in cohesionless soils. Int J Geomech 17(1):06016011. https://doi.org/10.1061/(ASCE)GM.1943-5622.0000689

Zhang WG, Li HR, Wu CZ, Li YQ, Liu ZQ, Liu HL (2021) Soft computing approach for prediction of surface settlement induced by earth pressure balance shield tunneling. Underground Space 6(4):353–363

Zhang W, Li Y, Wu C, Li H, Goh ATC, Liu H (2022) Prediction of lining response for twin tunnels constructed in anisotropic clay using machine learning techniques. Underground Space 7(1):122–133

Zheng G, Yang P, Zhou H, Zeng C, Yang X, He X, Yu X et al (2019) Evaluation of the earthquake induced uplift displacement of tunnels using multivariate adaptive regression splines. Comput Geotech 113:103099

Zhou H, Xu H, Yu X, Guo Z, Zheng G, Yang X et al (2021) Evaluation of the bending failure of columns under an embankment loading. Int J Geomech 21(7):04021112